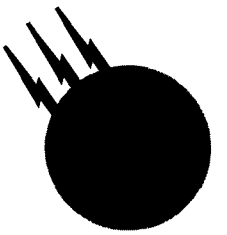

X-Ray Photoelectron Spectroscopy

Charles C. Chusuei
D. Wayne Goodman
Texas A&M University

GLOSSARY

Binding energy The energy (measured in eV) of the exiting *photoelectron* produced by the photoionization process of core level (first shell) electrons, which contain discrete chemical information. Peaks arising from energy level of various orbitals allow for qualitative oxidation state identification.

Core level shift Precise photoelectron binding energy peak positions of the peak centers denote the chemical oxidation and/or electronic states of orbitals from which the photoelectrons emanate. Minute variations in the binding energy arising from differing electronic environments of the ejected photoelectrons are manifested as shifts in the peak position (also referred to as *chemical shifts*).

Fermi level A reference point (taken as zero eV) with which binding energies of photoelectrons are measured.

Inelastic mean free path The average distance that a particle at a given energy (photoelectrons) can travel along a trajectory between inelastic collisions within a solid.

Intra- and extra-atomic relaxation The contraction of outer electronic orbitals toward the nucleus resulting from core hole vacancies following the photoemission process. The outgoing photoelectrons can be screened by either valence electrons within the atom (intra-atomic) or from local environment electrons just outside the atom (extra-atomic). These effects contribute to a surface analyte's core-level binding energy position observed in the X-ray photoelectron spectra.

Monolayer A one-molecule thick quantity of adsorbate on the surface.

Shake-up satellites Excitation of valence electrons (that accompanies relaxation processes) to an unfilled level at higher binding energy. The loss of kinetic energy of the outgoing photoelectron into a discrete

Encyclopedia of Physical Science and Technology, Third Edition, Volume 17

state appears as a peak along with the main core-level photoionization.

Surface sensitivity The ability to probe the topmost (on the order of angstroms) atomic layers of a solid.

Work function The energy required to remove an electron from the solid. This energy level above the Fermi reference is known as the *vacuum level.*

X-ray-excited Auger emission A secondary electron emission process that follows the photoionization and appears as a peak in the X-ray photoelectron spectrum. After the initial photoemission, an upper level valence electron relaxes into the vacant core-level state, followed by an ejection of another electron in the valence level.

X-RAY photoelectron spectroscopy (XPS) is an important and widely used surface analysis method in a many fields of study in physics and chemistry (e.g., microelectronics, heterogeneous catalysis, environmental geochemistry, etc.). The technique probes the energy distribution of electrons ejected from solids via irradiation by X-rays and the photoelectric effect; the electrons contain information regarding chemical oxidation state, electronic structure, and atomic composition of the analyte being studied. Thus, surface composition as well as the electronic environment can nondestructively (in many cases) be determined. X-ray photoelectron spectroscopy is also useful for quantitative analysis, capable of probing ultrathin layers of material (0.1% of a monolayer). Since the photoelectrons analyzed emanate only from the topmost atomic layers of the solid surface being studied ($\leq$100 Å), the technique is an invaluable tool for studying interfacial phenomena at the solid-solid and solid-gas boundaries.

I. FUNDAMENTALS OF XPS

A. The Photoelectric Effect and Secondary Processes

X-ray photoelectron spectroscopy (XPS) operates on the principle of the photoelectric effect, which occurs via a primary excitation process brought about by X-ray-irradiation producing electrons (*photoelectrons*) of discrete energy, containing chemical information regarding the surface analyte. It should be noted that X-rays are only one of many types of excitation sources that can be used to induce emission of electrons for analysis. X-ray photoelectron (XP) spectral peaks (generated by the photoelectrons) are named according to the orbital ($l = 0, 1, 2, 3 \ldots$ denoted as s, p, d, f. . .) and spin ($s = \pm 1/2$) quantum numbers of the core levels from which they emanate. The total momentum of the photoelectrons ($J = l \pm s$) is included in the nomenclature of a measured XP spectral peak (e.g., Ca $2p_{3/2}$ where $l + s = 1 + 1/2 = 3/2$).

The technique is sensitive to all elements except H and He and has a detection limit of about 0.1% of a monolayer. There is little systematic overlap of the spectral lines between elements albeit some does occur, such as Ca 2p/Au 3d, Pt 4f/Al 2p, O 1s, Sb 3d and Al 2s, 2p/Cu 3s, 3p. Difficulties arising from spectral overlap are easily overcome via examination of additional transitions (excitations) that can arise from the same element. In well-calibrated XPS systems, the precision of the quantitation measurements is typically within ±5%; thus, XPS is well-suited for both quantitative and qualitative elemental analysis.

In the photoemission process, an atom absorbs a photon of a known energy ($h\nu$) resulting in an ejection of a core level electron, which is detected and its energy measured. Figure 1 shows an energy level diagram relevant for binding energy measurements of a photoelectron escaping from the solid (sample specimen) and into the electron spectrometer. The conducting specimen is in electrical contact with the spectrometer housing so that both the sample and spectrometer have a common reference for measuring electron energy, called the *Fermi level*, E_F. Incoming photons (with energy $h\nu$) create a photoelectron with kinetic energy, E_k^1 relative to the *vacuum level*, E_v, of the sample. The kinetic electron energy at the sample surface, E_k^1, is determined from the kinetic energy of the electron, E_k, measured inside the spectrometer, from the relation:

$$E_k = E_k^1 - (\phi_{spec} - \phi_s) \tag{1}$$

where ϕ_{spec} and ϕ_s are *work functions* (energies required to remove electrons from the Fermi to vacuum levels) of the spectrometer and sample, respectively. From Fig. 1, it is evident that the binding energy of analyte from an electrically conducting sample may be obtained from the relation:

$$h\nu = E_b + E_k + \phi_{spec} \tag{2}$$

where $h\nu$ = photon energy from and an X-ray source and E_b = binding energy. Notably, ϕ_s is not involved in the measurement of the E_k that is "seen" by the spectrometer. In practice, the E_b of the incoming electrons is computed from the measured E_k from Eq. 2. Photoelectrons are generated via ejection from the solid surface upon excitation of core level orbitals by a photon source:

$$A + h\nu \rightarrow A^{+*} + e^- \text{ (photoelectron)} \tag{3}$$

where A is a neutral atom or molecule, A^{+*} is the excited ion and e^- is the ejected photoelectron. The photoionization along with competitive secondary processes are illustrated in Fig. 2. XPS owes its relatively nondestructive nature to the fact that only the ejection of electrons is

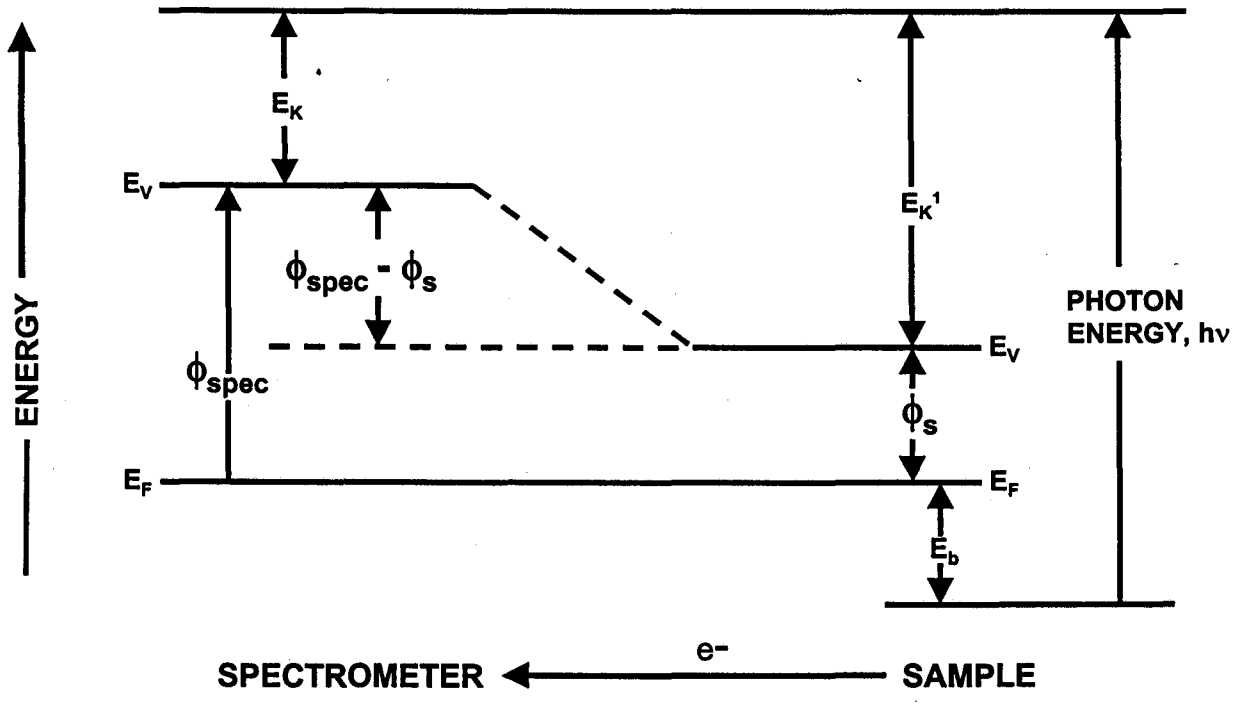

FIGURE 1 Energy level schematic for XPS binding energy measurements.

required for analysis. Unlike other techniques of elemental analysis, the atomic nuclei being examined remain unchanged during electron spectroscopic measurements. It should be noted that although some samples are sensitive to decomposition from exposure to the X-ray source, this is not generally intrinsic to the analysis technique. The photoionization is accompanied by two secondary emissions, characterized by either a photon emission resulting in *X-ray fluorescence*:

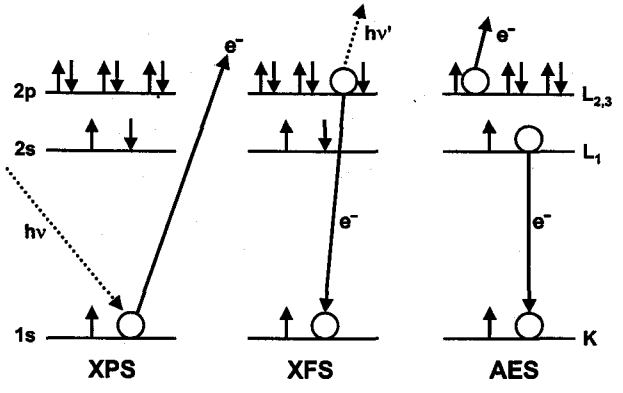

FIGURE 2 Diagrams depicting the photoemission process for XPS along with secondary emission processes (XFS and AES). [Reproduced with permission from the *Journal of Chemical Education*, Vol. 61, No. 6, 1984, p. 483; Copyright © 1984, Division of Chemical Education.]

$$A^{+*} \rightarrow A^{+} + h\nu' \text{ (X-ray photon)} \qquad (4)$$

or an ejection of a valence level electron, called an *Auger* electron, whose kinetic energy is independent of the photon energy:

$$A^{+*} \rightarrow A^{++} + e^{-} \text{ (Auger electron)} \qquad (5)$$

The initial photoionization is a two-step process, which can produce either Auger electrons or X-ray photons (i.e., fluorescence). X-ray fluorescence and Auger emissions are competitive processes. The Auger effect dominates for low-energy photoionization processes (about 1 kV) while X-ray emission dominates at high energies (about 10 keV). These secondary emissions are used for other surface analytical methods: X-ray fluorescence (XFS) and Auger electron (AES) spectroscopies. Since conventional XP spectrometers utilize a relatively low photon energy (i.e., Mg Kα at $h\nu = 1253.6$ eV; Al K$\alpha = 1486.6$ eV), contributions from fluorescence in the XP spectra are generally negligible. On the other hand, Auger transitions that are excited by the impinging X-ray photons commonly appear in XPS. X-ray-excited Auger electron spectroscopy (XAES) is innately a part of XPS, but is typically considered a separate technique because of the ways in which the data are analyzed. Figure 3 shows an XPS *survey scan* (0–1000 eV) of Ni deposited onto an H-ZSM-5 zeolite powder catalyst (DeGussa; consisting of mostly SiO_2) obtained using a Mg Kα source operated at 300 W. The XP

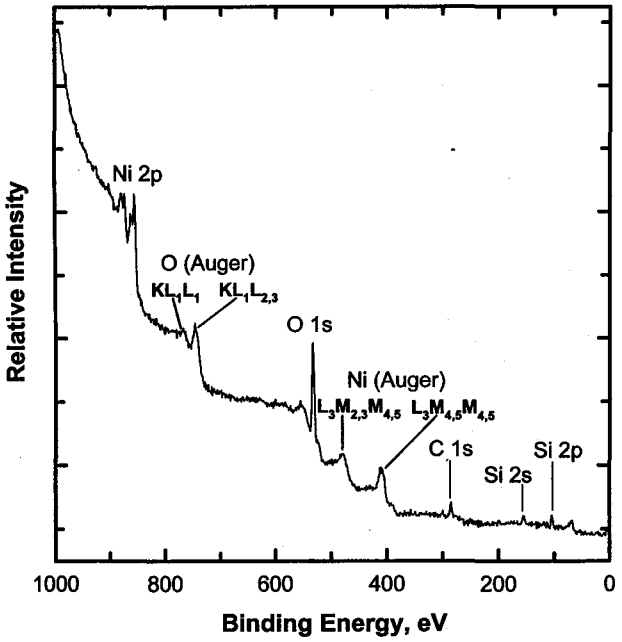

FIGURE 3 XP survey scan of Ni/H-ZSM-5 catalyst (DeGussa) containing O KLL and Ni LMM Auger transitions.

spectrum is a plot of the counting rate versus the binding energy of the detected photoelectrons. Other XPS core levels that are readily observed in the survey scan include those of the Ni 2p, C 1s, O 1s, and Si 2p orbitals. Different XPS transitions arising from various orbitals from a single element can appear at multiple peak positions in the survey scan. For example, Si has photoelectron transitions from the 2s and 2p levels that appear at about 150 and 100 eV (Fig. 3), respectively. Note that the high binding energy side of the XPS peak (e.g. O 1s, C 1s) has a higher background; this increase in count is due to partial loss of kinetic energy of the ejected electrons from inelastic collisions as it travels through the solid. Counts emanating from these partial losses have a reduced kinetic energy and would thus show up at higher binding energy in the XP spectrum (Eq. 2). The high background observed (Fig. 3) at about 900 eV extending up to the bombardment photon excitation energy is due to *bremmstralung* (German for "braking radiation") that is generated from the X-ray source.

The Auger effect is characterized by an upper level valence electron relaxation into the vacant core-level state (after the initial photoionization), followed by an ejection of another electron in the valence level. In the nomenclature of the Auger effect, for example, for the $KL_1L_{2,3}$ transition in Fig. 2, the first shell corresponds to the core level in which the initial vacancy was created (K) either via photoemission from XPS or electron impact bombardment from an electron beam, the second letter (shell) refers to the upper level valence electron that relaxes to fill the vacancy (L_1), and finally the third shell is the Auger electron that is ejected into the vacuum level ($L_{2,3}$) and then detected and measured via the spectrometer. Four groups of XAES lines are generated by conventional Mg Kα and Al Kα X-rays: (1) the KLL [Na, Mg, O, F, Mn, Fe, Co], (2) the LMM [Cu, Ni, Zn, Ga, Ge, As, Se], (3) the MNN [Ag, Cd, In, Sn, Sb, Te, Ru, Rh, Pd, I, Xe, Cs, Ba], and (4) the NOO [Au, Hg, Tl, Pb, Bi]. The X-ray-excited Auger peaks in Fig. 3, denoted by the arrows at the O KL_1L_1, O $KL_1L_{2,3}$, Ni $LM_{2,3}M_{4,5}$, and Ni $L_3M_{4,5}M_{4,5}$ transitions, typically have broader full-width half-maxima (fwhm) than the XPS lines (as compared to the fwhm of the O 1s, Ni $2p_{1/2}$, and $2p_{3/2}$ photoelectron emissions). Although too broad to be useful as indicators of chemical shifts, the Auger electron kinetic energy is independent of the primary excitation energy and can be used as reference points for detecting small chemical oxidation state changes (see Section III.A).

B. Properties of Solids and Surface Sensitivity

In order for electron spectroscopy to be effective, the ejected photoelectron has to "escape" from the solid, into the vacuum level, and finally into the electron energy analyzer and detector. Only electrons located near the top surface can escape without loss in kinetic energy because of the high probability of inelastic scattering inside the solid. Thus, XPS has severe limitations for studying bulk material. Surface compositions of materials can substantially differ from that inside the bulk due to segregation or surface contamination. On the other hand, the *surface sensitivity* of the technique (i.e., ability to probe the topmost atomic layers) is advantageous for studying interfaces and analyzing surface coverages that are only fractions of a monolayer thick. Thus XPS is valuable for the investigation of molecular-level adsorbates on solid surfaces. Figure 4 shows a "universal curve" plot of the *inelastic mean free path* (IMFP) versus the kinetic energy of the electron. The IMFP is defined as average distance that a particle (photoelectrons) can travel along a trajectory between inelastic collisions within a solid. The larger the kinetic energy, the longer the IMFP. In this particular plot, the IMFP of various elements (Ag, Au, Mo, Be, P, C, W) is given in angstrom units. A broad minimum IMFP is evident at 4–10 Å corresponding to a 10–500 eV electron kinetic energy. While photoionization occurs up to a few microns below the surface, only the electrons at the first few tens of angstroms exit the solid without energy loss and provide most of the intensity for XPS. As a rule of thumb, approximately 95% of the XPS signal arises from depths less than or equal to three times the IMFP.

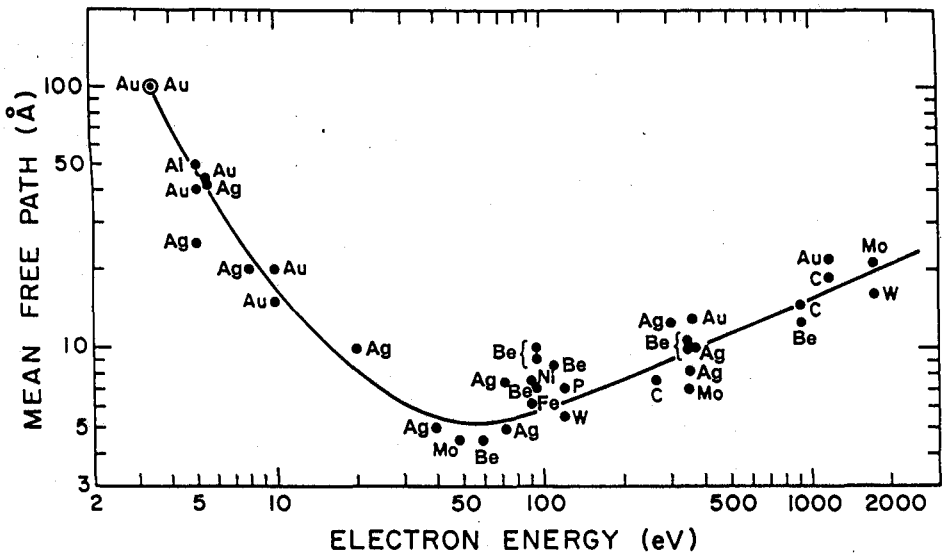

FIGURE 4 Universal curve plot of electron IMFPs of various elements. [Reprinted with permission from Somorjai, G. A. (1981). "Chemistry in Two Dimensions: Surfaces," p. 41, Cornell University Press, Ithaca, NY.]

II. INSTRUMENTATION

A. Ultrahigh Vacuum

A vacuum environment is necessary for XPS experiments to be undertaken for three reasons. First, low pressure is required to insure a sufficient inelastic mean free path for the photoelectrons to escape the solid and reach the electron detector without being dissipated via inelastic collisions. From the kinetic theory of gases, the mean free path of the gas molecule (analogous to the IMFP concept of photoelectrons traveling through a solid), λ', can be determined from

$$\lambda' = \frac{1}{d_0^2 n\sqrt{2}} \tag{6}$$

where d_0 = molecular diameter of the gas and n = density of molecules. In order for the technique to be effective, λ' must at least span the distance between the sample and analyzer, typically <1 m. Hence, in order to avoid dissipation via inelastic collisions of the escaping photoelectrons (or Auger electrons in the case of XAES), pressures of 10^{-5} Torr or lower are required. Second, even lower pressures (about 10^{-7} Torr; in the *high vacuum* pressure regime) are required to operate the X-ray anode and filaments without damage. Finally, in surface science experiments, low pressures are needed to minimize surface contamination from interfering with analysis. From the kinetic theory of gases, higher pressures accompany increased surface bombardment with gas molecules. Assuming a unity sticking coefficient, a 10^{-6} Torr pressure for 1 sec (defined as the unit, *Langmuir*) will produce a 1.0 monolayer of contamination. Thus, at 10^{-7} Torr the surface is contaminated after 10 sec, at 10^{-8} Torr the surface is contaminated after 100 sec, etc. Typically, pressures in the *ultrahigh vacuum* (UHV) regime (defined as 1×10^{-9} Torr or lower) are employed to maximize the analysis time before the surface is contaminated. To remove contamination, most systems are equipped with a means of *in situ* sample cleaning by *ion sputtering* and/or sample heating. Sputtering involves the bombardment of the substrate with a beam of an inert gas (such as He, Ar) to remove impurities via momentum transfer. Especially in the case of single crystal refractory metal substrates, sample heating for cleaning is typically accomplished by passing current through the specimen or electron beam (e-beam) bombardment. Temperatures as high as 2000 K can be readily achieved via e-beam heating.

B. Radiation Sources

In selecting an elemental source suitable for producing useful XP spectra, several factors need to be considered: (1) the energy resolution of the X-rays; (2) energy of the photons that are produced; and (3) ease of application of the material to an anode surface. Y Mζ ($h\nu = 132.3$ eV; fwhm = 0.47 eV) and Zr Mζ ($h\nu = 152.4$ eV; fwhm = 0.77 eV) lines produce photon energies that are too low in energy to be effective since they excite a narrow range of photoelectrons, which limits the number of elements that can be analyzed. Cu Kα ($h\nu = 8048$ eV; fwhm = 2.5 eV) has a sufficiently large excitation line to cover the full range of elements; however, its natural line width is too large (ideal fwhm <1.0 eV); this would limit

chemical oxidation state analysis due to poor spectral resolution. Si Kα produces a sufficiently high photon energy and narrow resolution to be a suitable X-ray source ($h\nu = 1739.5$ eV; fwhm = 1.00 eV). However, its insulating properties and difficulties associated with applying the material onto an anode surface make its use impractical. The Al Kα ($h\nu = 1486.6$ eV; fwhm = 0.85 eV) and Mg Kα ($h\nu = 1253.6$ eV; fwhm = 0.70 eV) lines suffer none of these limitations and are almost universally used in laboratory XPS instruments. Both have sufficient photon energy to excite characteristic lines of a wide range of elements and their natural line widths are sufficiently narrow to allow differentiation between multiple oxidation states. Both anodes produce XP spectra where overlap of photoelectron and X-ray-excited Auger lines can occur in certain photoelectron binding energy regions, complicating analysis. For this reason, most commercial systems produce X-ray sources with a dual anode system (e.g., Mg Kα/Al Kα). The XAES/XPS signal overlap of one anode is oftentimes not present when switching to the other anode for use. Both anodes can be used, respectively, during an experiment to eliminate these "blind spots."

It should be noted that while the Mg or Al radiation source is typically labeled with "Kα" for the sake of brevity, this unmonochromatized, "natural" line (spectrum) radiation is more complex. The X-ray lines (of each source) are an unresolved doublet, K$\alpha_{1,2}$, that have satellite features, K$\alpha_{3,4}$ and Kβ. Excitations from the K$\alpha_{3,4}$ and Kβ appear as satellites along side the photoelectron peak(s) produced by the K$\alpha_{1,2}$ and lead to spectral misinterpretation. K$\alpha_{3,4}$ excitations are ~10 eV on the low binding energy side of the main core-level peak and is approximately one-tenth of the K$\alpha_{1,2}$ intensity; Kβ excitations appear ~70 eV on the lower binding energy side. Removal of the satellites can be achieved via monochromatization of the X-ray source. These satellite intensities to some degree in nonmonochromatized systems are eliminated by using an aluminum foil X-ray window (approximately 8 μm thick) to reduce the bremsstrahlung radiation from the X-ray source.

Mg Kα and Al Kα radiation are typically excited with electron energy that is about 10 times greater than their respective photon energies (e.g., 15 kV, 300 W) for efficient production of photons. To insure optimum sensitivity and detection, the analyte surface is brought as close to the X-ray source as possible. Since a relatively large amount of energy is used to generate the X-ray source within a compact area (in which the X-ray anode is held), the anode must be kept sufficiently cool to avoid damage (to both the sample and anode). Deionized cooling water is typically used to transfer heat away from the anode (in thermal contact with a copper block). Conducting ions from the coolant fluid are removed chiefly for two reasons: (1) to avoid current generation that may be exhibited as artifacts in the XP spectrum and (2) as an electrical safety precaution due to the fact that the anode is typically operated at high voltage.

The drawback of using discrete line sources (as mentioned above) is that photoionization cross sections for different core levels excited by a fixed photon energy differ markedly; some cross sections will be at a maximum while others are at a minimum for the same line energy. Moreover, as discussed above there are severe limitations in the number of choices for other fixed line sources. The use of a continuously tunable source to circumvent this obstacle is available in the form of *synchrotron* radiation. In synchrotron, electrons are accelerated to near-relativistic speeds via pulsed magnetic fields around a circular ring, known as a *torus*, giving rise to X-ray irradiation. These electrons emit light in a continuous spectrum, having a shape dependent upon the radius of curvature and electron energy. Since the radiation is concentrated into a narrow cone tangential to the electron orbit, it can be easily passed into a monochromator for energy selection. Photon energies can be monochromatized to very high resolution in this manner. Another distinct advantage of using synchrotron radiation is that surface sensitivity can be tuned via adjusting the photon energy close to that of the photoionization threshold. Since the IMFP is proportional to the kinetic energy of the photoelectron, kinetic energies can be tuned to about 25–100 eV. The photoelectron signals thus obtained would have high surface sensitivity.

Synchrotron XPS systems are immense in size. The torus is typically tens of meters in diameter, providing energy and current outputs of several GeV and 1A, respectively. Stronger S/N is readily seen (as compared with single photon line XPS instruments) throughout the entire equivalent conventional XPS binding energy regime. In addition to the tunability of the X-ray source, the synchrotron radiation is 100% plane-polarized, pulsed, and has the advantage of allowing for time-resolved experiments to be performed. Due to its considerable expense in construction, repair, maintenance, and operation as well as the large space needed to house the apparatus, synchrotron XPS systems tend to be nationally owned and shared among numerous outside researchers. Thus, there are severely restricted time allowances available for experiments. Synchrotron instruments, due to their complexity, also tend to be out of operation for maintenance and repairs much more frequently than laboratory XPS instruments. Nevertheless, to many scientists the gains offered by a synchrotron source (not available to conventional laboratory XP spectrometers) warrant the inconvenience associated with its use.

C. Binding Energy Calibration

Since the XPS binding energy scaling may be compressed or expanded, points both at high and low binding energy bounds are needed in order to calibrate the entire binding energy span. The calibration procedure needs to be undertaken periodically to insure accurate binding energy measurements. This is typically accomplished with sputter-cleaned metal foils that are free of contaminants, such as carbon and oxygen. Energy positions of well-documented lines include Au $4f_{7/2}$ (84.0 eV; low) and Cu $2p_{3/2}$ (932.7 eV; high) are typically used. Binding energy peak centers of their respective photoelectron transitions are obtained via high-resolution narrow scans. The distance (i.e., scaling) between the high and low binding energy points is a parameter known as the *scale factor*, which can be controlled using the instrumental software. In practice, the scale factor is first adjusted and then followed by changing the *work function* [ϕ in Eq. (2)] to shift the entire binding energy scale so that the measured peaks match those of the standards. The work function adjustment oftentimes will change the scale factor and vice versa; thus, both variables should be changed taking into account the results of their interplay. This procedure thus requires multiple sets of XPS scans of high and low binding energy core levels. Figure 5 shows an XP survey scan of Au and Cu foils juxtaposed alongside each other; both the Au $4f_{7/2}$ and Cu $2p_{3/2}$ orbitals are thus readily accessible for instrumental calibration. Accompanying XAES Cu LMM features are also seen in the spectrum.

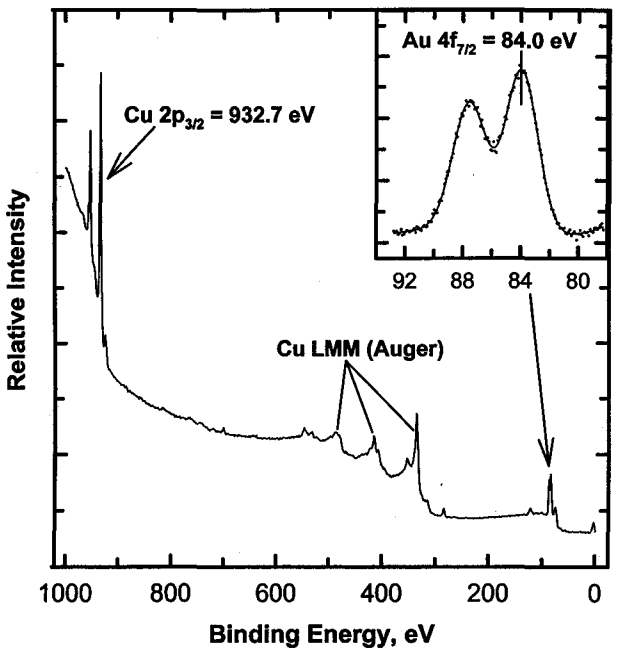

FIGURE 5 Sputter-cleaned Cu and Au foils (juxtaposed together on sample specimen holder). Binding energy peak positions of the Cu $2p_{3/2}$ and Au $4f_{7/2}$ levels serve as calibration standards. The inset shows an expanded view of the Au 4f orbital intensities.

D. Sample Charging

Many sample specimens have electrically insulating properties that would affect the XPS binding energy measurements and impede spectral interpretation. Sample *charging* occurs as a result of an accumulation of positive charge (as electrons are ejected away from the solid during photoemission) onto the surface when grounding of the sample (that would otherwise restore electrical neutrality) is impaired. For the nonconducting surface, electrons cannot return to the surface easily and are lost faster than they return. After a steady state is reached, a positive charge develops due to deficiency in electron density. Photoelectrons from the analyte would thus be ejected with a decreased kinetic energy (higher binding energy) along with broadening of the peak fwhm.

Corrections for charging can be accomplished by either (1) the use of reference standards or (2) an electron flood gun to neutralize the positive surface charge. One common practice is to evaporate Au *dots* onto the surface (after detailed high-resolution scans) and use the Au $4f_{7/2}$ level as the reference. In the case where the sample specimen has been exposed to atmospheric pressure, the C 1s line at 284.7 ± 0.2 eV denoting *adventitious carbon* (from hydrocarbons prevalent in the air) can be used. It should be noted that this type of correction may not adjust for changes in the scale factor due to *differential* (inhomogeneous) charging, i.e., some areas of substrate have more charge than others. In this instance, the charge correction for a high binding energy region of the XP spectrum may differ from that of a low one. A flood gun may be used instead to irradiate electrons to the sample specimen in order to neutralize charging. However, care should be taken in its use since many materials, especially organic substances, are sensitive to electron beam induced decomposition.

E. Energy Analyzers

X-ray photoelectron spectroscopy analysis allows for identification of various elements as well as differentiation of various chemical oxidation states. In order to accomplish these tasks, the energy resolution must be sufficiently high so that peaks from different chemical oxidation states can be deconvoluted. Furthermore, the resolution should remain relatively constant for all elemental transitions, i.e., the *absolute* resolution, ΔE, (defined by the fwhm) must remain the same. If the linewidths are to be matched by the absolute resolution at the maximum photon energies

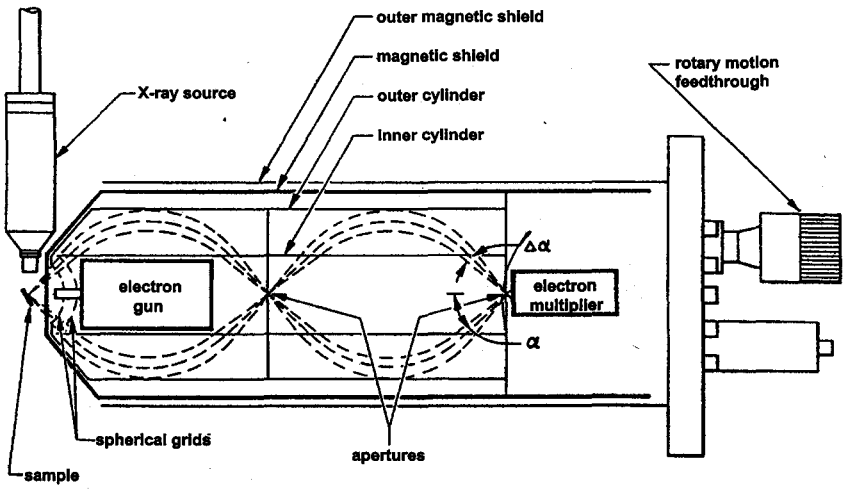

FIGURE 6 Double-pass cylindrical mirror analyzer for XPS and AES analysis. [Reproduced with permission from P. W. Palmberg, *Journal of Vacuum Science and Technology A*, Vol. 12, No. 1, 1975, p. 380; Copyright © 1975, American Institute of Physics.]

(e.g., fwhm = 0.70 eV for Mg Kα), a *relative* resolution (defined as $R = \Delta E/E_0$ where E_0 is the kinetic energy of the peak position) of $(0.70\ \text{eV} \div 1253.6\,\text{eV} =) 6 \times 10^{-4}$ would be required. Attaining this resolution is feasible but the data obtained herein would suffer unacceptable losses in sensitivity. In practice, the kinetic energies of the incoming photoelectrons (toward the detector) are retarded to a preselected analyzer energy and kept fixed during data acquisition. Thus, for a pass energy of 50 eV, the relative resolution needed would be $(0.70\ \text{eV} \div 50\,\text{eV} =) 1 \times 10^{-2}$, which can be easily achieved with minimal loss in sensitivity. Decreasing the pass energy effectively increases resolution. In the commonly used double-pass cylindrical mirror analyzer (CMA) setup (Fig. 6), two spherical grids at the front of the first stage are used to retard electrons (from the sample) entering the analyzer (and finally into the electron multiplier) when used in the XPS mode. The X-ray source is usually positioned as close as possible to the sample in this configuration. An electron gun is housed inside the CMA to excite Auger transitions. In some applications, the electron gun can also be modified for use as a flood gun to correct for charging. As a precaution, however, electron beam currents should not exceed 1×10^{-8} A since high currents can damage the electron multiplier. In an Auger electron spectrometer, only a single CMA is used to optimize the luminosity of the ejected Auger electrons. In this design for XPS, two CMAs are connected together in series to increase resolution; the exit aperture of the first stage is the entrance aperture to the second. Thus, the double-pass CMA evolved (i.e., from AES analysis) for use in XPS systems. In front of the first stage are spherical grids used to retard incoming photoelectrons at the preselected constant pass energy (by applying voltages to the inner and outer cylinders). Inner and outer magnetic shields depicted prevent external magnetic fields from altering the photoelectron flight path. The entrance angle into the CMA is fixed at $42.3 \pm 6°$. When the analyzer is used in the AES mode (best performed without retardation), these grids are grounded via a rotary motion feedthrough adjustment.

Unlike the CMA which was developed for use for both AES and XPS, the *concentric hemispherical analyzer* (CHA) was fabricated specifically for XPS since its inception. The CHA (Fig. 7) consists of two concentrically positioned hemispheres with inner (R_1) and outer (R_2) radii; ϕ and r are the angular and radial coordinates of the photoelectrons (with kinetic energy E_0) entering the analyzer at an entrance angle α. These spheres have negative and positive potentials, respectively, when voltages (V_0 and V) are applied across them. The median equipotentials between the hemispheres is found at radius, $R_0 = (R_1 + R_2)/2$. Similar to the CMA, it is customary to preretard the photoelectrons as they enter the analyzer. The angle of acceptance into the analyzer is adjustable. In the case where the angle (ϕ) between the entrance and exit aperture is 180°, as the incoming photoelectron travel across R_0 with kinetic energy, E_0, the deflecting potential, eV, varies with E_0 by

$$\text{eV} = E_0\left(\frac{R_2}{R_1} - \frac{R_1}{R_2}\right) \tag{7}$$

In order to optimize energy resolution, α can be adjusted so that $\alpha \approx \frac{w}{2R_0}$ where w = the slit width. Similar to the CMA system, photoelectrons are retarded to preselected pass energies via planar grids across the entrance slit as they enter

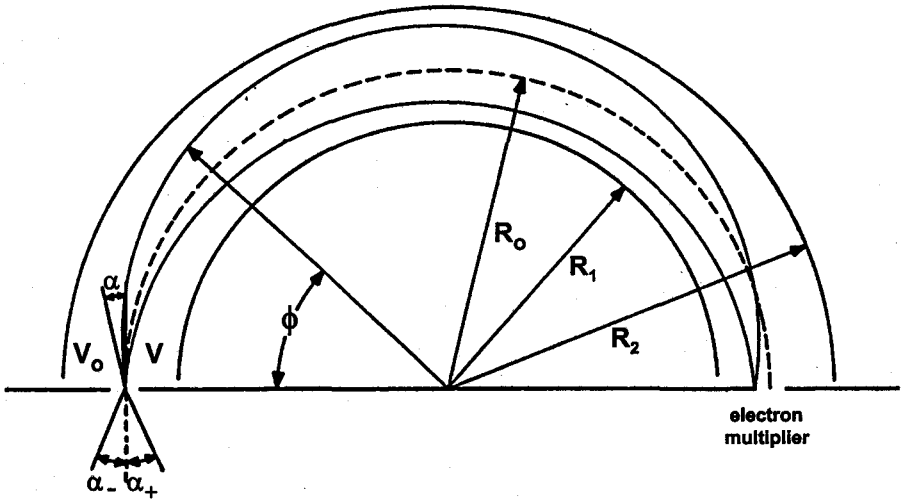

FIGURE 7 Concentric hemispherical analyzer (CHA) diagram. [Reproduced with permission from D. Roy and J.-D. Carette, *Canadian Journal of Physics*, Vol. 49, p. 2141, 1971; Copyright © 1971, NRC Research Press.]

the CHA. The CHA has the added option of the use of the lens system for improvement of overall efficiency of detection. The entrance slit to the CHA is narrow and one-dimensional, which gives the added advantage of *angle-resolved* analysis capabilities used for depth profiling the specimen.

F. Depth Profiling, Angle-Resolved Analysis

The sample specimen is rotated normal to the direction of the slit entrance to the CHA in order to adjust the surface-sensitivity of the analyte being sampled. Figure 8 shows a schematic depicting the relation between the IMFP, λ, and the average escape depth of the photoelectrons:

$$d = \lambda \sin \alpha \tag{8}$$

where d = the depth of the photoelectrons escaping from the solid and α = the *take-off* angle (angle between the flight of the photoelectrons from the solid and the surface itself). In this particular scenario, a more surface-sensitive depth is sampled, $d_1(\alpha_1 < 90°)$, in "A" as compared to $d_2\,(\alpha_2 \approx 90°)$ in "B"; decreasing the take-off angle increases surface sensitivity. In the case where the surface being analyzed consists of multiple layers (perhaps topmost layers have differing chemical oxidation states as compared to the bulk), a series of XPS scans performed varying the take-off angle would enable the surface and bulk components to be differentiated. By sampling the multiple layers via changing the surface specificity of the analysis in this manner, a *depth profile* of the top surface layers can be obtained. It should be noted that this type of analysis is only effective in the case in which the surface layers or thin films have thicknesses at the same order of magnitude as the IMFP, provided that the surface is flat. Angle-resolved analysis is not available with the CMA system due to its large solid angle, which impairs its ability to detect photoelectrons emanating from a single direction.

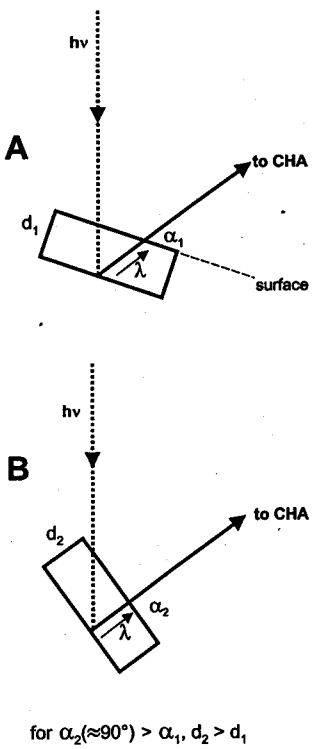

FIGURE 8 Angle-resolved analysis for depth profiling. Schematics show how surface sensitivity can be adjusted via changing the angle (α) of the path of ejected photoelectrons with respect to the CHA.

The single-dimensionality of the entrance slit also allows the added benefit for the CHA to be fitted with an input lens system.

III. ANALYSIS OF ELECTRONIC AND CHEMICAL STRUCTURE OF ATOMS, MOLECULES

A. Chemical Oxidation State Determination

Chemical shift data are typically obtained from high-resolution scans of smaller binding energy regions to determine precise peak center positions (also referred to as *narrow scans*). Small differences in the binding energy peak position (typically 0–3 eV) are attributed to chemical shifts arising from different electronic environments of the ejected photoelectrons. Variations in the number of valence electrons and the type of bonds they form (between neighboring atoms) influence the binding energy of the ejected photoelectrons, thus giving rise to chemical shifts exhibited in differences in the peak centers. Table I shows the chemical shifts (in eV) measured with respect to the zero oxidation state. Note that for each element depicted, as the oxidation number increases (becoming more positive), binding energy increases due to greater attraction of the nucleus to a core electron by the relative absence of outer valence electrons. When one of these outer shell electrons is removed, the effective charge sensed by the core electron increases (arising from a deficiency of electron density). Conversely, in the case where the attraction of the nucleus for a core electron is diminished by the presence of outer electrons, photoelectrons ejected from an electron-rich environment will exhibit a lower binding energy. Multiple oxidation states can appear in a given narrow scan. In order to make meaningful peak assignments to these different states, issues regarding instrumental resolution need to be addressed. In theory, the ΔE of a single oxidation state observed in an XP spectrum is a convolution of three components:

$$\Delta E = \sqrt{\Delta E_n^2 + \Delta E_p^2 + \Delta E_a^2} \tag{9}$$

where ΔE_n is the natural width of the core level, ΔE_p is the width of the photon source, and ΔE_a is the width from the analyzer resolution. Both ΔE_p and ΔE_a can be controlled experimentally by choosing an optimal photon source and varying instrumental settings of the analyzer, respectively. The photon line widths, ΔE_p, for standard Mg Kα and Al Kα sources are 0.70 and 0.85 eV, respectively, and are fixed values. ΔE_n, however, depends on the uncertainty of the core hole lifetime of the ionized state in the photoemission process. From the uncertainty principle, this natural line width can be expressed as:

$$\Delta E_n = \frac{\mathrm{h}}{\tau} = \frac{4.1 \times 10^{-15}}{\tau}\ \mathrm{eV} \tag{10}$$

where h = Planck's constant (eV · sec) and τ (sec) is the lifetime of the photoemission process. The fastest and slowest lifetimes vary between 10^{-15} to 10^{-13} sec, resulting in line widths with a lower and upper limits of 0.04 and 4 eV, respectively. Thus, based on the natural line widths, these fwhm values represent the upper and lower bounds of a single chemical oxidation state. In practice, the *absolute resolution* (ΔE) is obtained from by measuring the fwhm of an "ideal" photoelectron peak (from the analyte of interest) that is free from broadening effects or experimental artifacts (having a symmetrical Gaussian shape) and has the narrowest peak width in the XPS survey scan. The ΔE obtained can serve as a guide for deconvolution of multiple peaks when curvefitting spectra. For example, Fig. 9 shows an O 1s XPS peak separated into contributions from hydroxyl oxygen and the TiO_2 metal oxide oxygen. The curvefitting was not allowed to deviate from a 2.0–2.5 eV fwhm. The XP spectrum "A" shows the O 1s signal after a TiO_2 substrate was exposed to aqueous solution for

TABLE I Chemical Shifts as a Function of Oxidation State[a]

Element	Oxidation state									
	−2	−1	0	+1	+2	+3	+4	+5	+6	+7
Nitrogen 1s	—	*0[b]	—	+4.5[c]	—	+5.1	—	+8.0	—	—
Sulfur 1s	−2.0	—	*0	—	—	—	+4.5	—	+5.8	—
Chlorine 2p	—	*0	—	—	—	+3.8	—	+7.1	—	+9.5
Copper 1s	—	—	*0	+0.7	+4.4	—	—	—	—	—
Iodine 4s	—	*0	—	—	—	—	+5.3	—	—	+6.5
Europium 3d	—	—	—	—	*0	+9.6	—	—	—	—

[a] All shifts are measured in eV relative to the oxidation states denoted by the asterisks (*).
[b] Arbitrary zero measurement, end nitrogen in NaN_3.
[c] Middle nitrogen in NaN_3.
Reprinted with permission from Hercules, D. M. (1970). *Anal. Chem.* **42,** 28A; Copyright © 1970, American Chemical Society.

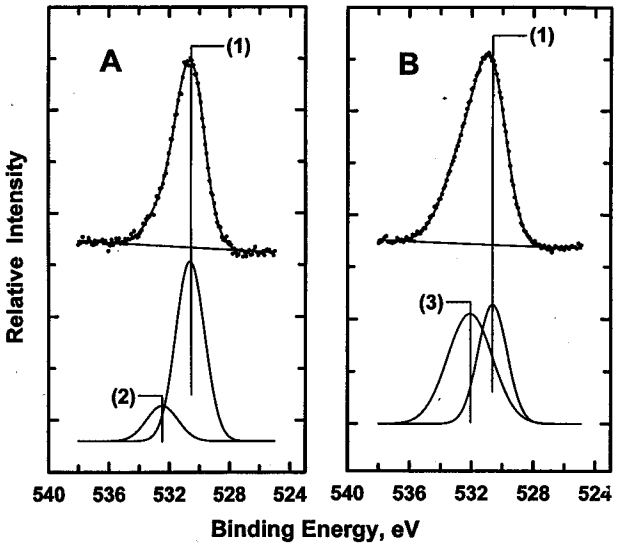

FIGURE 9 Deconvoluted O 1s XPS peaks of a TiO_2 substrate exposed to aqueous solution for (A) 10 min and (B) 12 hr. [Reproduced with permission from *Langmuir*, Vol. 15, No. 21, 1999, p. 7357; Copyright © 1999, American Chemical Society.]

10 min; spectrum "B" shows the same substrate after a 12-hr solution exposure. Deconvoluted peaks (1), (2), and (3) reveal different oxygen chemical environments arising from TiO_2, –OH, and H_2O, respectively. The contribution from –OH/H_2O increased with greater solution exposure time.

Chemical oxidation state identification from XAES features is accomplished using the concept of the *Auger parameter* (α), which is defined as the distance between the most prominent photoelectron emission and Auger features from the same element in an XP spectrum:

$$\alpha = E_k(\text{Auger}) - E_k(\text{PE}) \tag{11}$$

where E_k(Auger) and E_k(PE) are kinetic energies of the Auger and photoelectrons, respectively. In order to avoid negative α values and since $E_k(\text{PE}) = h\nu - E_b(\text{PE})$, Eq. (11) can be rearranged to:

$$\alpha + h\nu = E_k(\text{Auger}) + E_b(\text{PE}) \tag{12}$$

$$\alpha^* = E_k(\text{Auger}) + E_b(\text{PE}) \tag{13}$$

Thus, the *modified* Auger parameter (α^*; AP) is independent of the photon energy and is always positive. Since the AP is determined from energy differences rather than absolute energy measurements, its value is not affected by surface charging. The AP is therefore often more sensitive to chemical state changes than the photoelectron E_b peak centers. The AP varies inversely with the photon energy, i.e., the higher the $h\nu$ value, the lower the AP and vice versa. These AP data are typically plotted in two dimensions (Fig. 10). Since the AP data utilizes

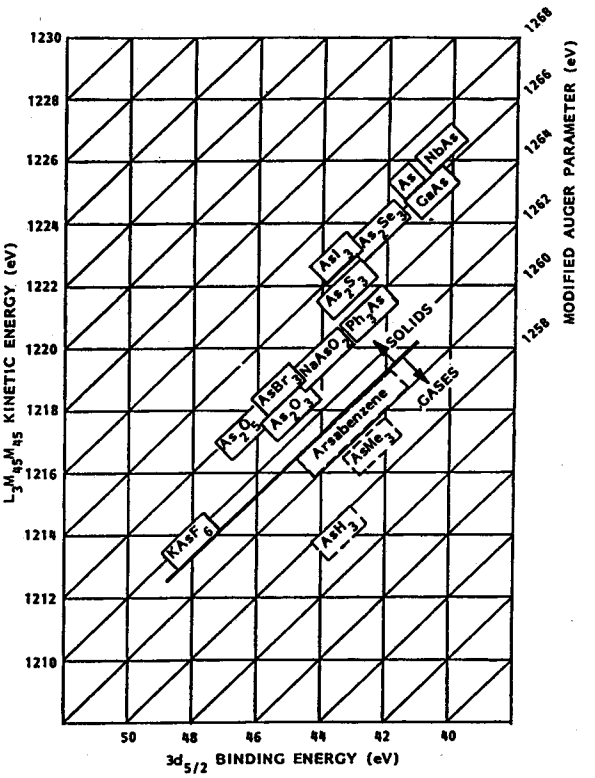

FIGURE 10 Modified Auger parameter plot. [Reprinted with permission from C. D. Wagner and A. Joshi, *Journal of Electron Spectroscopy and Related Phenomena*, Vol. 47, p. 301, 1988; Copyright © 1988, Elsevier Science.]

peak positions from both XPS and XAES, it is a particularly powerful means of differentiating various chemical oxidation states. The AP values are obtained via measured binding energy distances between the Auger transition (As $L_3M_{4,5}M_{4,5}$) and the core-level line (As $3d_{5/2}$). With this arrangement, the diagonal line represents equal sums of both Auger kinetic energy and XPS binding energy. The AP value can be obtained from the right-hand ordinate axis. It is noteworthy that while the original concepts of both α and α^* were empirical, they are directly related to extra-atomic relaxation energy (screening of outgoing Auger and photoelectron energy from neighboring atoms).

B. Quantitative Analysis

Assuming that the sample is homogeneous the number of photoelectrons per second (intensity) detected in an XP spectral peak is given by

$$I = n \cdot f \cdot \sigma \cdot \theta \cdot y \cdot \lambda \cdot A \cdot T \tag{14}$$

where n = number of atoms per cm^3 of the analyte, f is the X-ray flux in photons/$cm^2 \cdot$ sec, σ = the photoelectric cross section for the atomic orbital of interest in cm^2,

θ = the angular efficiency factor for the instrument, y = the efficiency of the photoelectric process (i.e., the probability a photon causes the ejection of a photoelectron), λ is the IMFP, A = the area of the analyte sample in cm^2, and T = the detection frequency. Equation (14) can be rewritten as:

$$n = \frac{I}{f \cdot \sigma \cdot \theta \cdot y \cdot \lambda \cdot A \cdot T} \tag{15}$$

The denominator term is defined as the *atomic sensitivity factor*, S, which differs for various elemental photoelectron transitions. Equation (15) can then be further extended to a generalized expression for determining the mole fraction of any constituent element from the sum of the peak intensities from all elements in the sample being analyzed:

$$C_x = \frac{n_x}{\sum_i n_i} = \frac{\frac{I_x}{S_x}}{\sum_i \frac{I_i}{S_i}} \tag{16}$$

where C is the concentration of analyte, x, of interest being scanned. The element, x, is a subset of all elements, i. Thus, given the measured absolute intensities of different core levels along with their respective sensitivity factors, the atomic percent composition of elements on the surface can be computed. It should be noted that this formula assumes a homogeneous distribution of elements throughout the sample. The structural model of the analyte needs to be known to insure accurate determinations of concentration. For example, an oxide thin film covering the topmost layers of a refractory metal substrate will attenuate underlying photoelectron signal while accentuating the relative oxygen intensity. Thus, the atom percent determination of the oxygen in this system would be an overestimation if the oxide overlayer structure is not taken into account.

C. Initial and Final State Effects

Koopmans' theorem predicts that the XP spectra observed represents the electronic states of electrons in the analyte atom before the photoemission process, i.e., the *initial* state. *Spin orbit coupling* is an example of an *initial* state effect, in which spectral features arise from the inherent unpaired electron make-up of the atoms prior to the photoemission event. In this scenario, peak splittings due to energy differences between singlet and triplet states via interaction of the spin and orbital magnetic moments occur whenever there are unpaired electrons in the valence shells. If the electron ejected is parallel (triplet state) to that of the valence electrons, it can undergo exchange interaction and result in a lower kinetic energy (higher binding energy) than the case for an anti-parallel spin (singlet state). The result is a doublet in the XP spectrum. Splittings due

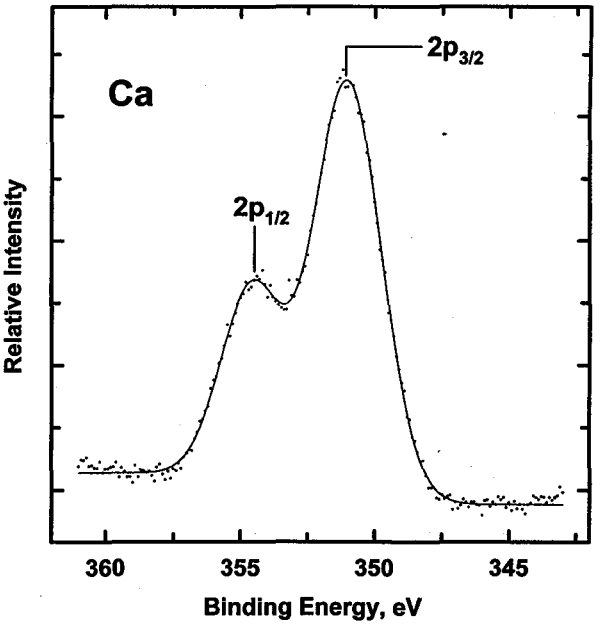

FIGURE 11 The XP spectrum of Ca 2p level showing spin-orbit-coupled $l \pm s = 1/2$ and 3/2 peaks.

to spin orbit coupling are generally not observed (resolved into 2 peaks) for low atomic number elements ($Z \leq 20$). A Ca 2p core level (Fig. 11), for instance, gives two photoemission peaks: $2p_{1/2}$ ($l = 1$ and $J = 1 - 1/2$) and $2p_{3/2}$ ($l = 1$ and $l = 1 + 1/2$). Similarly, d and f orbitals can split upon photoionization. The relative intensity ratio of the 2 peaks of a spin-orbit-coupled doublet is determined by the $2J + 1$ multiplicity of the levels. For example, the relative intensity of $J = 3/2$ and $J = 1/2$ components of a 2p is 4:2 = 2:1; for that of 5/2 and 3/2 peaks of a 3d level, it is 6:4 and for the 7/2 and 5/2 peaks of the 4f level, it is 8:6.

Binding energy shifts from initial state effects can be interpreted using the charge potential model:

$$E_b^i = kq_i + \sum_j \frac{q_i}{r_{ij}} + E_b^{ref} \tag{17}$$

where E_b^i = the binding energy of an electron from an atom i, q_i is the charge on the atom, k = constant, q_j = the charge on a neighboring atom j, r_{ij} = the distance between atom i and atom j, and E_b^{ref} = the energy reference. The kq_i term indicates that binding energy increases with increasing positive charge on the atom from which the photoelectron emanates. The $\sum_j \frac{q_j}{r_{ij}}$ term, known as the *Madelung* sum, in ionic solids negates the contribution from the kq_i term, since the neighboring atom has an opposite charge.

During the photoionization process, changes in the electronic environment due to the creation of the core-level vacancy leading to *final* state effects play a large role in influencing the binding energy. In order to properly

interpret the XPS binding energy value, perturbation of the electronic environment during the photoemission must be accounted for. For instance, let N = the number of total electrons in the atom before photoionization. The atom in its initial state conditions E_N^i absorbs a monochromatic photon of energy, $h\nu$, causing the ejection of a photoelectron with kinetic energy, E_k. The adsorption process takes place in approximately 10^{-17} sec. Approximately 10^{-14} sec later, the atom itself has one less electron and a core-level vacancy. The energy balance between initial and final states of the atom before and after photoionization can be expressed as:

$$E_N^i + h\nu = E_{N-1,l}^f + E_k \qquad (18)$$

where E_N^i = total energy of the atom with N electrons in the initial state (i.e., before photoionization), $E_{N-1,l}^f$ = the total energy of the atom with N-1 electrons and a hole in the core level, l, in the final state. It should be emphasized that the $N-1$ remaining electrons in the final state atom and electrons in neighboring atoms are influenced by the presence of the core shell vacancy, relaxing to lower the total energy of the of the atom by ΔE_{relax}. The relaxation energy should be accounted for in the determination of the kinetic energy of the photoelectron. The binding energy is not simply the energy of the orbital from which the photoelectron is emitted (i.e., initial state effect), but rather the difference in energy resulting from the perturbation of the remaining electrons upon removal of a core level electron. These photoemission processes occur at time scales sufficiently slow to influence exiting electrons via attraction of the core-ionized atom, known as the *adiabatic limit*. In the other extreme, photoelectrons can be emitted before the core-ionized atom relaxes. Photoemission during these "fast" processes (known as the *sudden limit*) often result in extra peaks in the XP spectrum. *Shake-up* and *shake-off* losses are final state effects which appear in the XP spectrum resulting from a photoelectron imparting energy to another electron within the atom. These features arise from the perturbation process (final state effects) caused by photoemission. The energy associated with relaxation may be sufficient to excite a valence level electron to higher energy. The electron receiving energy either ends up in a higher unoccupied state having discrete energy (shake-up) or an unbounded state (shake-off). Since photoemission and relaxation occur simultaneously, the outgoing photoelectron loses kinetic energy. These shake peaks, due to kinetic energy losses, appear at higher binding energy relative to the main core-level peak. Discrete shake-up losses are pronounced for metal oxides. Pronounced intensities are typically found for compounds having unpaired 3d or 4f electrons. Shake-up features that show up in the XP spectra of the Cu 2p core levels in Cu oxide stand out as a notable example (Fig. 12), providing noteworthy diagnostic tool for detecting the Cu^{2+}. The CuO spectrum shows pronounced shake-up satellite features (top) due to the fact that Cu^{2+} ($[Ar]3d^9$) has an open shell configuration. In contrast, Cu_2O (bottom) lacks these features since Cu^+ ($[Ar]3d^{10}$) has a closed shell arrangement.

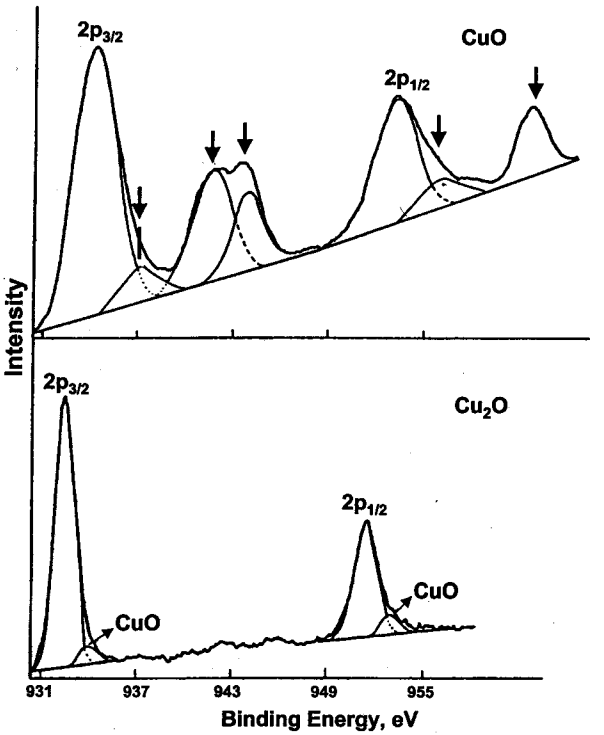

FIGURE 12 The XP scans of Cu 2p core levels of CuO (top) with pronounced shake-up satellites. [Reprinted from *Chemical Physics Letters*, Vol. 63, M. Scrocco, p. 53, Copyright © 1979, with permission from Elsevier Science.]

IV. EXAMPLES

The number of examples showing the utility of XPS, widely cited under many research journal titles, are too numerous to be included in a single encyclopedia article. Thus, only two illustrations are presented in this section with specific emphasis on applications for surface science studies to stimulate the reader's interest. Extensive reviews on the latest developments in the technique have been regularly published bi-annually on even-numbered years in *Analytical Chemistry*, a journal publication of the American Chemical Society. The *Journal of Electron Spectroscopy and Related Phenomena*, published by Elsevier, Amsterdam, is specifically devoted to the field of XPS as well as other electron spectroscopies. The first example addresses the use of XPS for characterizing the electronic

structure of the metal–metal bond in bimetallic systems; the second illustration is on the use of XPS to indirectly measure nanoscale CuO particle sizes.

A. Electron Donor-Electron Acceptor Interactions in Bimetallic Systems

In recent years, the electronic, chemical, and catalytic properties of bimetallic surfaces generated by vapor-depositing one metal onto a crystal face of a second metal has been the focus of considerable attention, motivated by the roles that bimetallic surfaces play in catalysis, electrochemistry, and microelectronics. Core-level binding energy shifts in bimetallic (transition metal) systems show that in the formation of the surface metal–metal bond, a gain in electrons by the element initially having a larger fraction of empty states in the valence band occurs. The trend observed, however, contradicts predictions based on the relative electronegativities of the bulk alloys. XPS thus shows that adsorbed surface metal atoms, called *adatoms*, have a different intrinsic electronic nature compared to bulk metal.

In the experiment, 1.0 monolayer (ML) coverages of Pd and Cu metal were deposited onto various single crystal transition metals via "hot" filament evaporation, followed by high-resolution XP scans. Figure 13 (top) shows the Pd $3d_{5/2}$ binding energy differences between the surface adatoms and that of bulk Pd for various supports. In all cases, the direction of the electronic perturbation for the Pd adatoms can be characterized with a model describing charge transfer from the Pd overlayer into the substrate. The magnitude of the electronic perturbation increases as the transition-metal substrate "moves" from right to left in the periodic table. For pseudomorphic Pd adatoms, the surface atomic density follows the order Ta(110), 1.30×10^{15} atoms/cm^2 < W(110), 1.42×10^{15} atoms/cm^2 ≈ Mo(110), 1.43×10^{15} atoms/cm^2 < Re(0001), 1.54×10^{15} atoms/cm^2 < Ru(0001), 1.57×10^{15} atoms/cm^2. Bimetallic systems with larger Pd–Pd bond distances (i.e., weaker Pd–Pd interactions) have stronger Pd-substrate interactions, thus resulting in larger electronic perturbations. In the case of Cu adatoms (Fig. 13, bottom), the binding energies are shifted either positively or negatively with respect to the bulk Cu value depending on the support. The bulk value for Cu was obtained from scans of the top layer of a Cu(100) crystal. The XPS data are consistent with a model in which Cu atoms supported on metals on the right side of the periodic table have electron densities larger than that of Cu(100) surface atoms. Similarly, a reverse phenomenon is observed for Cu atoms supported on metals on the left side of the periodic table. For pseudomorphic Cu monolayers, the surface atomic density

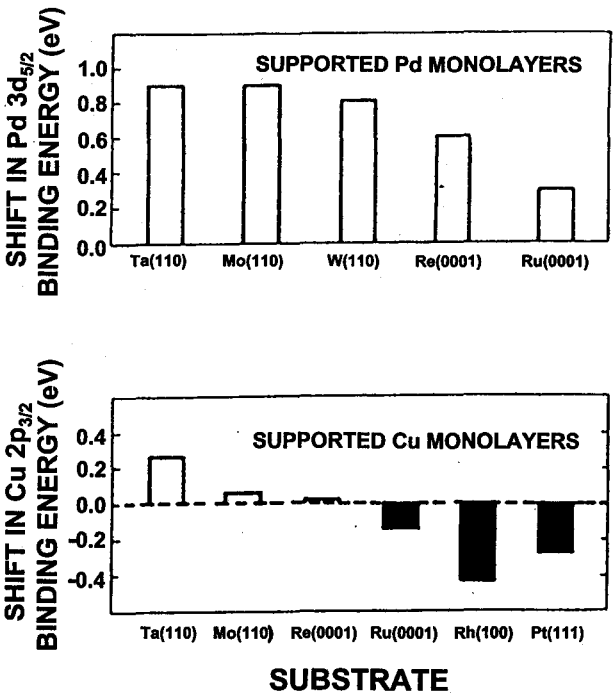

FIGURE 13 Top: Difference in Pd $3d_{5/2}$ XPS binding energy between 1.0 ML Pd and surface atoms of Pd(100) as a function of metal substrate. Bottom: Difference in Cu $2p_{3/2}$ XPS binding energy between 1.0 ML Cu and surface atoms of Cu(100) as a function of metal substrate. [Reproduced with permission from *The Journal of Physical Chemistry*, Vol. 95, No. 15, 1991; Copyright © 1991, American Chemical Society.]

follows the sequence: Ta(110) < Rh(100), 1.38×10^{15} atoms/cm^2 < Mo(110) < Pt(111),1.51×10^{15} atoms/cm^2≈ Re(0001) < Ru(0001) (Fig. 13, bottom). Thus, similar to Pd, bimetallic systems with the larger Cu–Cu adatom bond distances have the larger overlayer-substrate interactions.

Trends seen for both Pd and Cu adlayers can be explained by a simple model that takes into account the type of metals present. The strongest electronic perturbations are found for systems that involve a combination of a metal with an almost fully occupied valence band and a metal with a valence band more than half empty. The formation of a surface metal–metal bond generally leads to a gain in electron density by the element initially having the larger fraction of empty states in its valence band. The direction of electron transfer can be easily understood in terms of orbital mixing: hybridization of the occupied states of an electron-rich metal A with the unoccupied levels of an electron-deficient metal B. This mixing leads to a loss of A character in the occupied states and hence a reduction in the electron density on metal A. In the case of Pd (an electron-rich admetal), the relative core-level shift of the 1.0 ML of the Pd $3d_{5/2}$ level (with respect to the

bulk value) supported on various transition metals similarly follows the trend: Ta > W > Re > Ru. The core-level shift decreases in the left-to-right direction of the periodic table. The magnitude of the perturbations induced by the loss of electron density increases as the fraction of empty levels in the valence band of the metal substrate increases: Ta > W > Re > Ru (Fig. 14a). Cu, on the other hand, has a 4s valence band that is half empty and can act as either an electron donor or acceptor, depending upon the fraction of empty states in the valence band of the metal substrate.

Interestingly, there is an excellent correlation between the changes in the admetal binding energies and the relative abilities of these transition-metal substrates to adsorb Pd as measured by temperature programmed desorption (TPD), which can also be explained using the model described above. [The TPD technique involves adsorbing the analyte metal onto a substrate followed by linearly heating the sample to desorb it and subsequent detection via mass spectrometer. A plot of the ion current (mass spectral intensity) is obtained as a function of temperature. The peak temperature maximum of the resulting spectrum is indicative of the admetal binding strength to the surface.] Desorption temperatures of Pd monolayers from several surfaces are presented in Fig. 14b. These data show a general trend of stronger Pd-substrate bond strengths for elements with the least occupied valence band. The Pd/Ta(110) system has a desorption temperature of 1540 K, the highest observed, and the Pd/Ru(0001) has the lowest desorption temperature (1440 K). The larger the electronic perturbations on the Pd atoms, the stronger the bimetallic bond. An interrelationship between the magnitude of the Pd $3d_{5/2}$ core level shift and the Pd-substrate binding strength is thus readily observed. Similarly, a strong correlation has been found between changes in the XPS core-level binding energies and variations in the ability for the supported films to adsorb CO. Temperature programmed desorption data indicate CO desorption temperatures from $Pd_{1.0ML}$/Ta(110) (~250 K), $Pd_{1.0ML}$/W(110) (~300 K), $Pd_{1.0ML}$/Ru(0001) (~330 K) that are much lower than that from Pd(100) (~480 K). According to the above-described model, the electron density of supported monolayers of Pd is smaller than that of the surface atoms of Pd(100). A partial positive charge on the Pd adatoms is consistent with a reduction in their ability to coordinate CO via π–back–bonding, producing a weaker Pd—CO bond on the supported monolayers compared to Pd(100). The model described above predicts that the Pd surface atom electron density and ability to π–back–donate will follow the sequence $Pd_{1.0ML}$/Ta(110) < $Pd_{1.0ML}$/W(110) < $Pd_{1.0ML}$/Ru(0001) < Pd(100). This exact trend is exhibited in the TPD data. For monolayers of Cu (having a relatively electron-deficient density) deposited on electron-rich metals (Ru, Rh, and Pt), the model predicts an enhancement in electron density and π–back–bonding capacity of the Cu adatoms with respect to the surface atoms of Cu(100). Adsorption of CO on Cu films induces a large increase in the Cu $2p_{3/2}$ XPS binding energy, in part, due to π–back–donation. Figure 15 illustrates how the CO-induced shift in the Cu $2p_{3/2}$ peak position (measured after saturating the Cu surfaces with CO at 100 K) changes with the metal substrate. The CO—induced shift increases as the metal substrate "moves" from left to right in the periodic table. This trend is attributed to an increase in the ability of the Cu adatoms to π–back–donate.

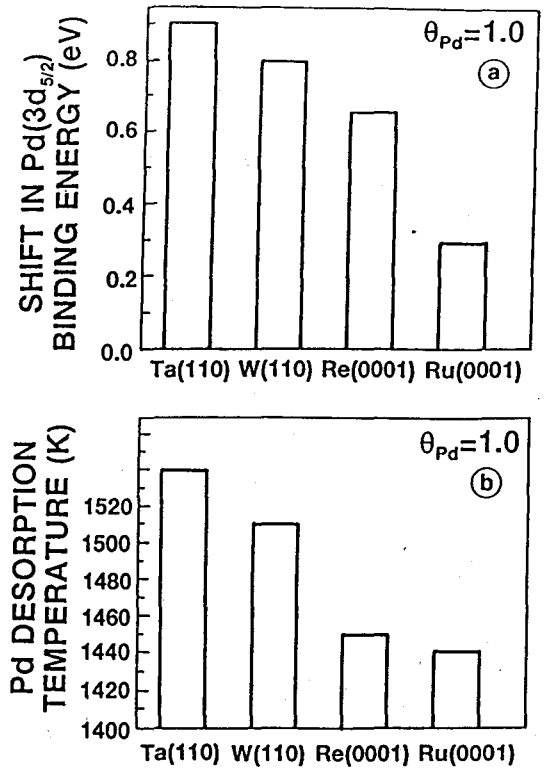

FIGURE 14 (a) Binding energy shift in Pd $3d_{5/2}$ level for 1.0 ML Pd on several single crystal substrates relative to the surface atoms of Pd(100). (b) The TPD desorption peak temperature maxima of 1.0 ML Pd deposited on several substrates. [Reprinted with permission from *Physical Review B*, Vol. 46, No. 1, p. 7082, 1992; Copyright © 1992, American Physical Society.]

B. Finite Size Effects on Core-Level-to-Shake-up Satellite Intensities

Surface characterization of CuO particles supported on SiO_2 is a catalyst system of importance for industrial applications, such as the synthesis of methanol. X-ray photoelectron spectroscopy has been shown to be an

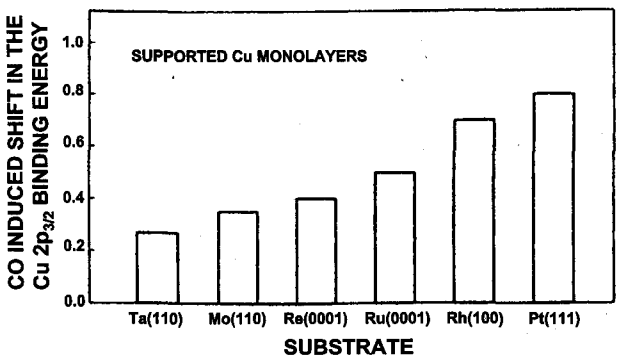

FIGURE 15 CO-induced XPS binding energy shifts of the Cu $2p_{3/2}$ level measured after saturation the 1.0 ML Cu/metal substrate surfaces with CO at 100 K. [Reproduced with permission from *The Journal of Physical Chemistry*, Vol. 95, No. 15, 1991; Copyright © 1991, American Chemical Society.]

effective tool for indirectly measuring CuO particle size in the Cu/SiO_2 system.

In the experiment, the CuO/SiO_2 model catalyst was prepared by depositing $Cu(CH_3CO_2)_2 \bullet H_2O$ [$Cu(ac)_2$] dissolved in butanol onto an SiO_2 support via spin-coating. The SiO_2 substrate with this adlayer was then calcinated to 450°C to remove unwanted organic substituents and hence form spherically shaped CuO particles. The particle sizes were varied via changing the $Cu(ac)_2$ solution concentrations. Four size distributions were produced with mean particle heights (corresponding to mean diameter) of 3.7, 4.1, 4.4, and 6.3 nm, formed from concentrations of 0.0040 *M*, 0.0070 *M*, 0.0085 *M*, and 0.010 *M* $Cu(ac)_2$, respectively. These dimensions were verified using atomic force microscopy (AFM).

Figure 16A shows a stackplot of XP spectra of the Cu 2p core regions acquired from these surfaces after AFM imaging. Shake-up features at ~945 and ~965 eV for the Cu $2p_{3/2}$ and $2p_{1/2}$ core levels are evident and are diagnostic of an open $3d^9$ shell of Cu(+2). The peak positions and relative intensities of the satellites from these levels are indicative of the presence of CuO at the surface. The relative intensities of the shake-up lines to the main core level of both the Cu $2p_{3/2}$ and $2p_{1/2}$ levels varied as a function of $Cu(ac)_2$ solution concentration. The shake-up intensities denoting CuO on the surface were relatively more intense at higher $Cu(ac)_2$ concentration.

The peakfit of the Cu $2p_{3/2}$ core level revealed two binding energy states (with fwhm in parentheses) at 932.8 (1.91) and 933.8 (3.12) eV, which we assign to a Cu(0/+1) state and CuO, respectively. The binding energy region scanned to obtain these Cu 2p peaks (925–975 eV) took approximately 40 min to acquire. It was during this acquisition time that X-ray irradiation from XPS caused reduction of the CuO particles. For the smaller CuO particles, the ratio of exposed surface area to bulk is greater, which

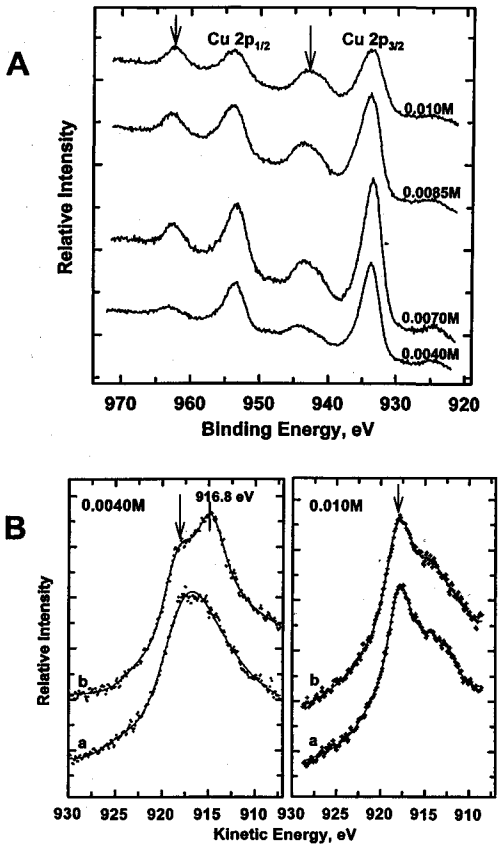

FIGURE 16 (A) The XPS of Cu $2p_{1/2}$ and $2p_{3/2}$ peaks of varying particle sizes of CuO on SiO_2 prepared from various $Cu(ac)_2$ concentrations; (B) The XAES of Cu LMM spectra upon (a) immediate XP scans and (b) after a 50 min X-ray exposure. [Reproduced with permission from *Langmuir*, Vol. 15, No. 8, 1999, p. 2807; Copyright © 1999, American Chemical Society.]

results in an overall increased dosage of X-ray irradiation and hence greater susceptibility to reduction. In addition, the presence of adventitious carbon obtained from treating these substrates in air likely enhanced reduction. From our XPS measurements of the C 1s level intensities and taking into account atomic sensitivity factors for all of the orbitals scanned (including O 1s, Cu $2p_{3/2}$ and Si 2p), there was 12–25 atom percent carbon on these surfaces. Further, XPS induced reduction of Cu(+2) to Cu(+1) has been reported to increase in the presence of carbonaceous overlayers.

To test this hypothesis of particle size dependent reduction rates, the Cu $L_3M_{4,5}M_{4,5}$ XAES regions were examined before and after exposure of the substrates to the soft X-rays. Figure 16B shows Auger spectra of the Cu $L_3M_{4,5}M_{4,5}$ transition of 0.010 *M* and 0.0040 *M* $Cu(ac)_2$ prepared surfaces corresponding to the largest and smallest CuO particle sizes, respectively. Spectra "a" of both samples were taken immediately after initial X-ray irradiation and "b" after 50 additional min of exposure to

the X-ray gun. Instrumental parameters and X-ray exposure times were identical for both particle sizes scanned. The arrows at 917.8 eV denote the XAES peak position of CuO, which is consistent with the literature. No difference in the Auger line shape or position was seen in the 0.010 *M* $Cu(ac)_2$ prepared sample; however, a marked difference was seen for the 0.0040 *M* substrate before and after the 50-min X-ray exposure. Even upon initial exposure to the X-ray source, a difference in the Auger line shapes can be seen between the two particle sizes in spectra "a". This difference in the Auger line shape between spectrum "a" of the 0.0040 *M* $Cu(ac)_2$ and that of 0.010 *M* $Cu(ac)_2$ indicates that some reduction has already taken place during this initial scan. After 50 min, a feature at 916.8 eV in spectrum "b" of the 0.0040 *M* $Cu(ac)_2$ substrate, which is assigned to a Cu(+1) state (Cu_2O), dominates. Some intensity within this spectral region can be seen in "a" but is relatively weak compared to the 917.8 eV position. No intensity was observed within the 918.8 eV Cu $L_3M_{4,5}M_{4,5}$ region corresponding to that reported for metallic Cu(0). It can thus be concluded that Cu(0) is not present on the surface and that the CuO particles are likely reduced to Cu_2O. Clearly, there is greater reduction for the smaller particles.

Figure 17A shows a representative peakfit of the Cu $2p_{3/2}$ core level and its corresponding shake-up satellites. This particular fit is for the 0.0040 *M* $Cu(ac)_2$ treated sample that exhibited the largest core-level intensity due to Cu(+1). Gaussian line shapes with a linear background were used to fit peak 1, which is assigned to the Cu(+1) state; peaks 2, 3, and 4 are assigned to the Cu(+2) state. The ratio of the sum of the areas of peaks 2, 3, and 4 to that of peak 1 was used as a measure of the relative amount of Cu(+2) to Cu(+1) on the surface. As the Cu oxide particle size increases, the relative amount of XPS-induced reduction decreases. Intensity from Cu(+2) dominated in XP scans of larger particles (6.3 nm) while intensity from Cu(+1) dominated in XP scans of smaller ones (3.7 nm); in addition, there was a decrease in the Cu 2p shake-up intensity (Fig. 16A). Figure 17B shows a plot of $[Cu^{+2}]/[Cu^{+}]$ calculated from the above-mentioned peak areas as a function of the AFM-measured cluster heights of the CuO particles; $[Cu^{2+}]/[Cu^{+}]$ varies linearly and increases with particle size.

These examples represent only a glimpse into the numerous applications of XPS to obtain information (both qualitative and quantitative) regarding the chemical oxidation state, atomic composition, and electronic structure of surfaces. When used in combination with complementary surface analytical probes (such as TPD and AFM as illustrated in the preceding examples), XPS can be an especially powerful technique for obtaining a detailed picture of the solid-solid/solid-gas interface. For further examples and discussion of the broad scope of applications offered by XPS, the reader is referred to the supporting literature cited in the captions of the figures and bibliography section.

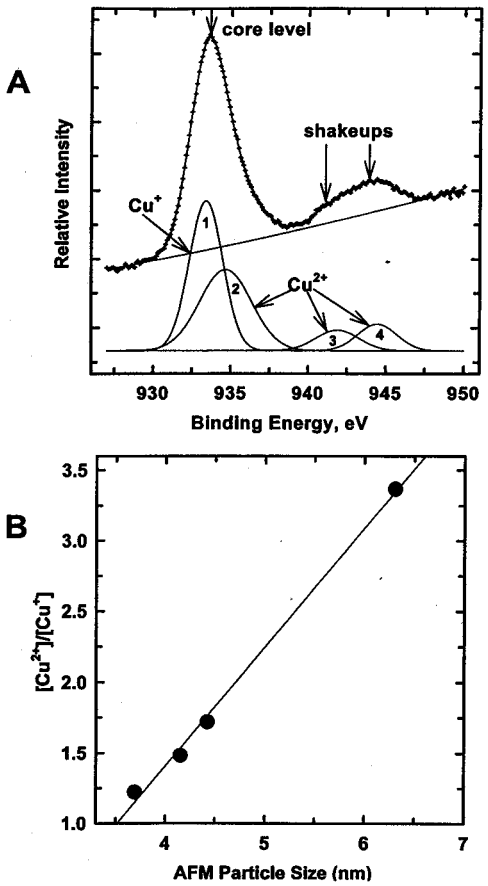

FIGURE 17 (A) Curvefit of XPS Cu $2p_{3/2}$ core level. Peak 1 denotes the binding energy state for Cu(+1). Peaks 2–4 denote the Cu(+2) state; (B) Plot of $[Cu^{2+}]/[Cu^{+}]$ from XPS Cu $2p_{3/2}$ peak areas as a function of particle size using AFM measured cluster height. [Reproduced with permission from *Langmuir*, Vol. 15, No. 8, 1999, p. 2808; Copyright © 1999, American Chemical Society.]

SEE ALSO THE FOLLOWING ARTICLES

AUGER ELECTRON SPECTROSCOPY • MOLECULAR ELECTRONICS • PHOTOELECTRON SPECTROSCOPY • SURFACE CHEMISTRY • VACUUM TECHNOLOGY • X-RAY ANALYSIS • X-RAY, SYNCHROTRON RADIATION AND NEUTRON DIFFRACTION

BIBLIOGRAPHY

Barr, T. L., and Seal, S. (1995). Nature and use of adventitious carbon as a binding energy standard. *J. Vacuum Sci. Technol. A* **13**, 1239–1246.

Briggs, D. (1998). "Surface Analysis of Polymers by XPS and Static SIMS," Cambridge Univ. Press, Cambridge, U.K.

Henrich, V. E., and Cox, P. A. (1996). "The Surface Science of Metal Oxides," Cambridge Univ. Press, Cambridge, U.K.

Hüfner, S. (1996). "Photoelectron Spectroscopy: Principles and Applications, 2nd edition," Springer-Verlag, Berlin.

Oleford, I. (1997). X-ray photoelectron spectroscopy. *In* "Surface Characterization: A User's Sourcebook" (D. Brune, R. Hellborg, H. J. Whitlow, and O. Hunderi, eds.), pp. 291–319. Wiley-VCH Verlag, Weinheim, Germany.

Powell, C. J., Jablonski, A., Tilinin, I. S., Tanuma, S., and Penn, D. R. (1999). Surface sensitivity of Auger-electron spectroscopy and X-ray photoelectron spectroscopy. *J. Electron Spectrosc. Related Phenomena* **98–99,** 1–15.

Somorjai, G. A. (1994). "Introduction to Surface Chemistry and Catalysis," Wiley, New York.

Turner, N. H., and Schreifels, J. A. (2000). Surface analysis: X-ray photoelectron spectroscopy and Auger electron spectroscopy. *Anal. Chem.* **72,** 99R–110R.

Woodruff, D. P., and Delchar, T. A. (1994). "Modern Techniques of Surface Science, 2nd edition," Cambridge Univ. Press, Cambridge, U.K.